Frontiers of Information Technology & Electronic Engineering
www.jzus.zju.edu.cn; engineering.cae.cn; www.springerlink.com
ISSN 2095-9184 (print); ISSN 2095-9230 (online)
E-mail: jzus@zju.edu.cn

Waveform design based on mutual information upper bound for joint detection and estimation[*]

Ruofeng YU, Chenyang LUO, Mengdi BAI, Shangqu YAN, Wei YANG, Yaowen FU[†‡]
College of Electronic Science and Technology, National University of Defense Technology, Changsha 410073, China
[†]E-mail: fuyaowen@nudt.edu.cn

Received Apr. 29, 2025; Revision accepted Sept. 22, 2025; Crosschecked Oct. 29, 2025; Published online Nov. 27, 2025

Abstract: Information-theoretic principles provide a rigorous foundation for adaptive radar waveform design in contested and dynamically varying environments. This paper addresses the joint optimization of constant modulus waveforms to enhance both target detection and parameter estimation concurrently. A unified design framework is developed by maximizing a mutual information upper bound (MIUB), which intrinsically reconciles the tradeoff between detection sensitivity and estimation accuracy without heuristic weighting. Realistic, potentially non-Gaussian statistics of target and clutter returns are modeled using Gaussian mixture distributions (GMDs), enabling tractable closed-form approximations of the MIUB's Kullback–Leibler divergence and mutual information components. To tackle the ensuing non-convex optimization, a tailored metaheuristic phase-coded dream optimization algorithm (PC-DOA) is proposed, incorporating hybrid initialization and adaptive exploration–exploitation mechanisms for efficient phase-space search. Numerical results substantiate the proposed approach's superiority in achieving favorable detection estimation trade-offs over existing benchmarks.

Key words: Radar waveform design; Mutual information upper bound; Target detection; Parameter estimation; Constant modulus constraint
https://doi.org/10.1631/FITEE.2500276 **CLC number:** TN957

1 Introduction

Modern radar systems are fundamental to defense, autonomous navigation, and environmental monitoring (Skolnik, 2008). Their performance, quantified by detection probability, estimation accuracy, and spatiotemporal resolution, is dictated by the transmitted waveform (Levanon and Mozeson, 2004). The advent of cognitive radar has shifted waveform design from static libraries to adaptive, context-aware strategies (Haykin, 2006), a capability essential for multifunction radars operating in congested and contested spectra (Guerci et al., 2014).

Waveform design for detection has traditionally followed the Neyman–Pearson (NP) criterion, though its direct implementation is hindered by the complexity of the likelihood ratio test (LRT). Surrogate measures, including signal-to-clutter-plus-noise ratio (SCNR) (Xu et al., 2022, 2025a), deflection coefficients (Zhu et al., 2017), and entropy-based divergences (Tang et al., 2015; Xu et al., 2025b), have therefore been widely adopted in advanced architectures such as frequency diverse array (FDA) (Gui et al., 2018) and multiple-input multiple-output (MIMO) radars (Tang et al., 2018). For parameter estimation (range, Doppler, and direction of arrival), classical analyses have shown that waveform properties determine accuracy through the Fisher information matrix (FIM) (DeLong and Hofstetter,

---

[‡] Corresponding author

[*] Project supported by the National Natural Science Foundation of China (No. 61871384), the Science Fund for Distinguished Young Scholars of Hunan Province (No. 2024JJ2066), and the Science and Technology Innovation Program of Hunan Province (No. 2022RC1092)

ORCID: Ruofeng YU, https://orcid.org/0000-0002-5189-736X; Yaowen FU, https://orcid.org/0000-0001-7081-266X

© Zhejiang University Press 2025

1970). Accordingly, designs often minimize Cramér–Rao lower bounds (CRLB) (van der Werf et al., 2023) or maximize mutual information (MI) (Bell, 1993; Idriss et al., 2021).

In practice, detection and estimation are interdependent, motivating joint optimization. Multi-objective formulations (Jiu et al., 2015; Hao et al., 2019; Shen et al., 2024; Yu et al., 2024) provide partial solutions, while learning-based approaches (Thornton et al., 2020) suffer from complexity and generalization issues. Information-theoretic designs have been explored, e.g., a two-stage scheme using MI and Kullback–Leibler (KL) divergence (Xiao and Hu, 2022), yet a unified foundation remains lacking. To address this gap, a variational framework based on the MI upper bound (MIUB) is established. The MIUB decomposes into an MI term that captures estimation fidelity and a KL divergence term characterizing detection separability, thus balancing the two objectives without requiring heuristic weighting. The main contributions are as follows:

1. Unified variational framework: Joint detection-estimation waveform design is formulated via MIUB maximization, unifying MI- and KL-based criteria.

2. Flexible statistical modeling: Gaussian mixture distributions (GMDs) are adopted for target and clutter, combining fidelity with analytical tractability.

3. Phase-coded dream optimization algorithm (PC-DOA): A constant modulus synthesis algorithm with hybrid initialization and adaptive dynamics is developed to enhance convergence and solution quality.

2 Signal model and problem formulation

This section establishes the mathematical framework for the radar system. Specifically, it introduces the signal model and formulates the waveform optimization problem for the joint enhancement of target detection and parameter estimation.

2.1 Signal model

We consider a monostatic radar transmitting a discrete-time baseband waveform $\boldsymbol{s} = [s_1, s_2, \ldots, s_N]^{\mathrm{T}} \in \mathbb{C}^N$, where N denotes the waveform length. The received signal $\boldsymbol{y} \in \mathbb{C}^{N+N_{\mathrm{T}}-1}$ is modeled by the following binary hypothesis test:

$$\begin{cases} \mathcal{H}_0: & \boldsymbol{y} = \boldsymbol{w}, \\ \mathcal{H}_1: & \boldsymbol{y} = \boldsymbol{S}\boldsymbol{x} + \boldsymbol{w}, \end{cases} \tag{1}$$

where $\boldsymbol{x} \in \mathbb{C}^{N_{\mathrm{T}}}$ represents the stochastic target impulse response (TIR) with length N_{T}, $\boldsymbol{w}$ represents the clutter-plus-noise process, and $\boldsymbol{S} \in \mathbb{C}^{(N+N_{\mathrm{T}}-1)\times N_{\mathrm{T}}}$ is the Toeplitz convolution matrix generated by $\boldsymbol{s}$, whose elements are

$$[\boldsymbol{S}]_{i,j} = \begin{cases} s_{i-j+1}, & 1 \le j \le N_{\mathrm{T}}, \\ & j \le i \le j+N-1, \\ 0, & \text{otherwise}. \end{cases} \tag{2}$$

To capture the non-Gaussian and heavy-tailed statistics commonly observed in high-resolution radar returns, the target response $\boldsymbol{x}$ and the clutter-plus-noise vector $\boldsymbol{w}$ are modeled as zero-mean GMDs, obtained by

$$p(\boldsymbol{x}) = \sum_{m=1}^{M} \beta_m \mathcal{CN}(\boldsymbol{x}; \boldsymbol{0}, \boldsymbol{Q}_m), \tag{3}$$

$$p(\boldsymbol{w}) = \sum_{k=1}^{K} \alpha_k \mathcal{CN}(\boldsymbol{w}; \boldsymbol{0}, \boldsymbol{R}_k), \tag{4}$$

where M and K represent the numbers of mixture components associated with the target and clutter models, respectively. $\mathcal{CN}(\cdot; \boldsymbol{\mu}, \boldsymbol{\Sigma})$ is the complex Gaussian probability density function (PDF) and $\{\beta_m, \boldsymbol{Q}_m\}$ and $\{\alpha_k, \boldsymbol{R}_k\}$ are the mixture parameters, subject to $\sum_{m=1}^{M} \beta_m = 1$ and $\sum_{k=1}^{K} \alpha_k = 1$. The corresponding likelihoods of $\boldsymbol{y}$ under $\mathcal{H}_0$ and $\mathcal{H}_1$ are also GMDs, obtained by

$$p_0(\boldsymbol{y}) \triangleq p(\boldsymbol{y}|\mathcal{H}_0) = \sum_{k=1}^{K} \alpha_k \mathcal{CN}(\boldsymbol{y}; \boldsymbol{0}, \boldsymbol{R}_k), \tag{5}$$

$$p_1(\boldsymbol{y}) \triangleq p(\boldsymbol{y}|\mathcal{H}_1) = \sum_{\ell=1}^{L} \gamma_\ell \mathcal{CN}(\boldsymbol{y}; \boldsymbol{0}, \boldsymbol{\Sigma}_\ell), \tag{6}$$

with $L = MK$, $\gamma_\ell = \alpha_k \beta_m$ for the mapping $\ell \leftrightarrow (k, m)$, and

$$\boldsymbol{\Sigma}_\ell = \boldsymbol{S}\boldsymbol{Q}_m\boldsymbol{S}^{\mathrm{H}} + \boldsymbol{R}_k. \tag{7}$$

Clearly, the covariance matrices $\boldsymbol{\Sigma}_\ell$ depend explicitly on the waveform $\boldsymbol{s}$, establishing a direct link between waveform design and radar performance.

Remark 1 Gaussian mixture models provide a flexible yet analytically tractable framework, serving as universal approximators that can accurately represent heavy-tailed clutter and compound target statistics. Their adoption is well supported in radar waveform design, where they have demonstrated strong modeling fidelity and robustness for both measured and simulated data (Blacknell, 2000; Gu and Goodman, 2019; Chen et al., 2023).

2.2 Problem formulation

The objective is to design the waveform $\boldsymbol{s}$ under the constant modulus constraint as follows:

$$|s_n| = c = \sqrt{E_\mathrm{s}/N}, \quad n = 1, 2, \ldots, N, \tag{8}$$

where E_s denotes the total transmitted energy.

Instead of employing heuristic scalarizations of detection and estimation criteria, we adopt the MIUB as a unified design metric (Poole et al., 2019). The MIUB is defined as

$$\mathrm{MIUB}(\boldsymbol{s}) \triangleq \mathbb{E}_{p(\boldsymbol{x})}\left[\mathcal{D}_{\mathrm{KL}}(p_1(\boldsymbol{y} \mid \boldsymbol{x}) \parallel p_0(\boldsymbol{y}))\right], \tag{9}$$

where $p_1(\boldsymbol{y} \mid \boldsymbol{x})$ denotes the conditional PDF under $\mathcal{H}_1$ hypothesis.

Lemma 1 (MIUB decomposition) The MIUB admits the decomposition as follows:

$$\mathrm{MIUB}(\boldsymbol{s}) = \underbrace{I(\boldsymbol{x};\boldsymbol{y})}_{\mathfrak{E}(\boldsymbol{s})} + \underbrace{\mathcal{D}_{\mathrm{KL}}(p_1(\boldsymbol{y}) \parallel p_0(\boldsymbol{y}))}_{\mathfrak{D}(\boldsymbol{s})}, \tag{10}$$

where $I(\boldsymbol{x};\boldsymbol{y})$ measures estimation fidelity, while the KL divergence quantifies detection separability.

Maximizing the MIUB provides a rigorous framework for the joint optimization of detection, $\mathfrak{D}(\boldsymbol{s})$, and estimation, $\mathfrak{E}(\boldsymbol{s})$, within an information-theoretic setting. This formulation naturally encapsulates the trade-off between discriminative capability and estimation accuracy. However, the exact evaluation of Eq. (10) under GMD likelihoods is generally intractable due to the non-analytic nature of the differential entropy terms and the high-dimensional integrals involved. To circumvent this computational challenge, we adopt the following tractable approximation strategies.

Lemma 2 (MI approximation (Gu and Goodman, 2019)) The MI term can be approximated as

$$\overline{\mathfrak{E}}(\boldsymbol{s}) = \Xi\left(\{\alpha_k, \boldsymbol{R}_k\}_{k=1}^{K}\right) - \Xi\left(\{\gamma_\ell, \boldsymbol{\Sigma}_\ell\}_{\ell=1}^{L}\right), \tag{11}$$

where the function Ξ is defined as

$$\Xi\left(\{\pi_i, \boldsymbol{C}_i\}_{i=1}^{I}\right) \triangleq \ln\left(\sum_{i=1}^{I} \pi_i (\det(\boldsymbol{C}_i))^{-1}\right), \tag{12}$$

with weights $\pi_i > 0$, $\sum_{i=1}^{I} \pi_i = 1$, and $\boldsymbol{C}_i$ denoting covariance matrices.

Lemma 3 (KL divergence approximation (Goldberger et al., 2003)) The KL divergence term admits the following approximation as

$$\overline{\mathfrak{D}}(\boldsymbol{s}) = \sum_{\ell=1}^{L} \gamma_\ell \left[\ln \frac{\gamma_\ell}{\alpha_{k^\star(\ell)}} + \mathcal{L}(\boldsymbol{\Sigma}_\ell, \boldsymbol{R}_{k^\star(\ell)})\right], \tag{13}$$

where

$$k^\star(\ell) = \arg\min_{k} \mathcal{L}(\boldsymbol{\Sigma}_\ell, \boldsymbol{R}_k) \tag{14}$$

is the best-matching component in p_0 and the function $\mathcal{L}$ is defined as

$$\begin{aligned}\mathcal{L}(\boldsymbol{A}, \boldsymbol{B}) &\triangleq \mathcal{D}_{\mathrm{KL}}\big(\mathcal{CN}(\boldsymbol{0}, \boldsymbol{A}) \parallel \mathcal{CN}(\boldsymbol{0}, \boldsymbol{B})\big) \\ &= \mathrm{tr}\left(\boldsymbol{B}^{-1}\boldsymbol{A}\right) - \ln\det\left(\boldsymbol{B}^{-1}\boldsymbol{A}\right) - n',\end{aligned} \tag{15}$$

where $\mathrm{tr}(\cdot)$ and $\det(\cdot)$ denote the trace and determinant of a matrix, respectively. $\boldsymbol{A}$ and $\boldsymbol{B}$ denote generic covariance matrices and $n' = N + N_\mathrm{T} - 1$.

Remark 2 A concise error analysis of the approximations in Lemmas 2 and 3 is presented in Appendix A. The results demonstrate that the proposed surrogate formulations are theoretically sound and yield controllable approximation errors under specific assumptions, such as low variance in MI and well-separated components in the KL divergence.

By combining these approximations, the final optimization problem is formulated as

$$(\mathcal{P}_1): \begin{array}{ll} \max_{\boldsymbol{s}} & F(\boldsymbol{s}) \triangleq \overline{\mathfrak{E}}(\boldsymbol{s}) + \overline{\mathfrak{D}}(\boldsymbol{s}) \\ \text{s.t.} & |s_n| = c, \quad n = 1, 2, \ldots, N, \end{array} \tag{16}$$

where

$$\begin{aligned} F(\boldsymbol{s}) = \sum_{\ell=1}^{L} \gamma_\ell \Bigg[&\ln \frac{\gamma_\ell}{\alpha_{k^\star(\ell)}} + \mathrm{tr}\left(\boldsymbol{R}_{k^\star(\ell)}^{-1} \boldsymbol{\Sigma}_\ell\right) \\ &- \ln\left(\boldsymbol{R}_{k^\star(\ell)}^{-1} \boldsymbol{\Sigma}_\ell\right) - (N + N_\mathrm{T} - 1)\Bigg] \\ &+ \ln\left[\sum_{k=1}^{K} \alpha_k \boldsymbol{R}_k^{-1}\right] - \ln\left[\sum_{\ell=1}^{L} \gamma_\ell \boldsymbol{\Sigma}_\ell^{-1}\right]. \end{aligned}$$

It should be noted that the objective function $F(\boldsymbol{s})$ defined in $(\mathcal{P}_1)$ is Lipschitz continuous according to the following proposition.

Proposition 1 Assume that all component covariance matrices $\{\boldsymbol{R}_k\}_{k=1}^{K}$ and $\{\boldsymbol{Q}_m\}_{m=1}^{M}$ have eigenvalues contained in $[\lambda_{\min}, \lambda_{\max}]$ with $0 < \lambda_{\min} \leq \lambda_{\max} < \infty$, and that the mixture weights satisfy

$\min\{\alpha_k, \beta_m, \gamma_\ell\} > 0$. Under the constant modulus constraint $|s_n| = c$ $(n = 1, 2, \ldots, N)$, the objective $F(\boldsymbol{s})$ is globally Lipschitz continuous on $\mathcal{M} = \{\boldsymbol{s} \in \mathbb{C}^N : |s_n| = c, \forall n\}$. That is, there exists a constant $L_{\mathrm{F}} < \infty$ such that

$$|F(\boldsymbol{s}_1) - F(\boldsymbol{s}_2)| \le L_{\mathrm{F}} \|\boldsymbol{s}_1 - \boldsymbol{s}_2\|_2, \ \forall \boldsymbol{s}_1, \boldsymbol{s}_2 \in \mathcal{M}, \quad (17)$$

where the constant L_{F} depends only on $\lambda_{\min}$, $\lambda_{\max}$, N, the mixture weights, the modulus c (equivalently the total energy E_{s}), and the structural dimensions N_{T}, K, and M.

Proof See Appendix B for details.

The resulting problem $(\mathcal{P}_1)$ is inherently nonconvex due to both the objective function $F(\boldsymbol{s})$ and the constant modulus feasible set, necessitating the development of specialized global optimization strategies, as detailed in Section 3.

3 Proposed PC-DOA

The optimization problem $(\mathcal{P}_1)$ in Eq. (16) is inherently challenging due to two primary sources of non-convexity: (1) the objective function $F(\boldsymbol{s})$, which involves logarithmic determinant terms in $\overline{\mathfrak{D}}(\boldsymbol{s})$ and $\overline{\mathfrak{E}}(\boldsymbol{s})$, and (2) the feasible set $\mathcal{M}$, imposed by the constant modulus constraint. These factors yield a highly intricate landscape with numerous local extrema. Conventional gradient-based methods are unsuitable in this setting, as gradients are computationally expensive to obtain and offer no guarantee against poor local solutions.

To overcome these difficulties, we propose the PC-DOA, a metaheuristic specifically designed for MIUB-based waveform design under constant modulus constraints. PC-DOA circumvents the need for gradient information by employing a population-based search enhanced with problem-specific mechanisms, including hybrid initialization and adaptive phase updates.

3.1 Phase-coded representation

The constant modulus condition $|s_n| = c$ is enforced by parameterizing the feasible set as the complex circle manifold:

$$\mathcal{M} = \left\{\boldsymbol{s} \in \mathbb{C}^N : |s_n| = c, \ \forall n\right\}. \quad (18)$$

Any $\boldsymbol{s} \in \mathcal{M}$ can be uniquely expressed via a phase vector $\boldsymbol{\theta} = [\theta_1, \theta_2, \ldots, \theta_N]^{\mathrm{T}} \in [-\pi, \pi)^N$ as

$$\boldsymbol{s}(\boldsymbol{\theta}) = c \cdot \left[\mathrm{e}^{\mathrm{j}\theta_1}, \mathrm{e}^{\mathrm{j}\theta_2}, \ldots, \mathrm{e}^{\mathrm{j}\theta_N}\right]^{\mathrm{T}}. \quad (19)$$

This representation inherently satisfies the modulus constraint and reduces the search space to $\boldsymbol{\theta}$. To ensure $\boldsymbol{\theta}$ remains within $[-\pi, \pi)$ during updates, we define a periodic wrapping operator $\Psi : \mathbb{R}^N \to [-\pi, \pi)^N$ as

$$[\Psi(\boldsymbol{\theta})]_n = \mathrm{mod}(\theta_n + \pi, 2\pi) - \pi, \quad (20)$$

where $\mathrm{mod}(a, b)$ returns values in $[0, b)$. Each update is passed through $\Psi(\cdot)$, embedding the constraint directly into the representation and eliminating the need for explicit projection steps.

3.2 Hybrid initialization strategy

The effectiveness of population-based metaheuristics critically depends on the quality and diversity of the initial population. To accelerate convergence while mitigating premature stagnation, PC-DOA adopts a hybrid initialization scheme. For a population size of N_{p}, we generate $\{\boldsymbol{\theta}_i^0\}_{i=1}^{N_{\mathrm{p}}}$ through three complementary mechanisms.

3.2.1 LFM-inspired initialization

To exploit the favorable structure of linear frequency modulation (LFM) signals, $N_{\mathrm{LFM}} = \lfloor \eta N_{\mathrm{p}} \rfloor$ individuals are seeded with LFM-like phase patterns with $\eta \in (0, 1)$. The n^{th} component of the i^{th} such individual is defined as

$$[\boldsymbol{\theta}_{\mathrm{LFM},i}^0]_n = \Psi\left(\beta_i \pi \frac{(n-1)^2}{N-1} + \Delta_{i,n}\right), \quad (21)$$

with $\beta_i \sim \mathcal{U}(-1, 1)$ denoting a random chirp-rate parameter and $\Delta_{i,n} \sim \mathcal{U}(-\Delta, \Delta)$ a small perturbation $(\Delta \ll \pi)$, where $\mathcal{U}(a, b)$ denotes the continuous uniform distribution over $[a, b)$.

3.2.2 Chaotic initialization

To promote broad exploration, $N_{\mathrm{chaos}} = \lfloor (N_{\mathrm{p}} - N_{\mathrm{LFM}})/2 \rfloor$ individuals are generated using the Logistic map. Starting from $\boldsymbol{\rho}^0 \in (0, 1)^N$, the dynamics evolve as

$$\rho_n^k = 4\rho_n^{k-1}(1 - \rho_n^{k-1}), \quad (22)$$

where $k = 1, 2, \ldots, K_{\mathrm{chaos}}$.

The resulting sequence is mapped to phases via

$$[\boldsymbol{\theta}_{\mathrm{chaos},i}^0]_n = \Psi\left(-\pi + 2\pi\rho_n^{K_{\mathrm{chaos}}}\right). \quad (23)$$

3.2.3 Random initialization

The remaining $N_{\rm rand} = N_{\rm p} - N_{\rm LFM} - N_{\rm chaos}$ individuals are initialized uniformly at random:

$$[\boldsymbol{\theta}^0_{{\rm rand},i}]_n \sim \mathcal{U}(-\pi, \pi). \tag{24}$$

This tripartite strategy combines structural priors, chaotic diversity, and uniform randomness, yielding a well-balanced initialization that supports rapid convergence and robust exploration.

3.3 Exploration and exploitation

The optimization in PC-DOA proceeds as an iterative refinement process that balances global exploration and local exploitation. Let $\mathcal{P}_t = \{\boldsymbol{\theta}^t_1, \boldsymbol{\theta}^t_2, \ldots, \boldsymbol{\theta}^t_{N_{\rm p}}\}$ denote the population at iteration t. The fitness of each candidate $\boldsymbol{\theta}^t_i$ is evaluated as

$$f(\boldsymbol{\theta}^t_i) = F(\boldsymbol{s}(\boldsymbol{\theta}^t_i)) = \overline{\mathfrak{D}}(\boldsymbol{s}(\boldsymbol{\theta}^t_i)) + \overline{\mathfrak{E}}(\boldsymbol{s}(\boldsymbol{\theta}^t_i)), \tag{25}$$

where $\overline{\mathfrak{D}}(\cdot)$ and $\overline{\mathfrak{E}}(\cdot)$ are defined in Eqs. (13) and (11), respectively, and $\boldsymbol{s}(\boldsymbol{\theta})$ is parameterized in Eq. (19). The search process is divided into two stages, determined by the iteration index t relative to the maximum budget T.

3.3.1 Exploration phase

In the early stage ($t \leq \alpha T$, with $\alpha \approx 0.9$), the algorithm emphasizes broad exploration. The population $\mathcal{P}_{t-1}$ is partitioned into G subgroups $\mathcal{G}_1, \mathcal{G}_2, \ldots, \mathcal{G}_G$. Within each subgroup $\mathcal{G}_g$, the local elite is identified as

$$\boldsymbol{\theta}^{\rm best}_g = \mathop{\arg\max}_{\boldsymbol{\theta} \in \mathcal{G}_g} f(\boldsymbol{\theta}). \tag{26}$$

Candidate solutions are updated via stochastic perturbations on a random subset of dimensions. For $\boldsymbol{\theta}_{\rm old} \in \mathcal{G}_g$, the number of perturbed entries is

$$k \sim \mathcal{U}_{\rm int}\left(\left\lceil \frac{N}{8G} \right\rceil, \left\lceil \frac{N}{7G} \right\rceil, \ldots, \left\lceil \frac{N}{3G} \right\rceil\right), \tag{27}$$

where $\mathcal{U}_{\rm int}$ denotes the discrete uniform distribution, and $\lceil t \rceil$ denotes the ceiling function, i.e., the smallest integer greater than or equal to t. For $n \in \mathcal{I}$, the update rule is expressed as

$$[\boldsymbol{\theta}_{\rm new}]_n = \Psi\left([\boldsymbol{\theta}_{\rm old}]_n + \zeta(t) \cdot \Delta_n\right), \tag{28}$$

with $\Delta_n \sim \mathcal{U}(-\pi, \pi)$ and a time-decaying step-size factor

$$\zeta(t) = \frac{1}{2}\left(\cos\left(\frac{\pi t}{T}\right) + 1\right). \tag{29}$$

Unperturbed entries remain unchanged. This subgroup-based mechanism preserves diversity while mitigating premature convergence.

3.3.2 Exploitation phase

In the later stage ($t > \alpha T$), the focus shifts to local exploitation around the global best solution. Let $\boldsymbol{\theta}^{\rm global}$ denote the best solution obtained thus far. For each $\boldsymbol{\theta}_{\rm old}$, a random subset $\mathcal{I}$ of at most $k_{\max} = \max(2, \lceil N/3 \rceil)$ dimensions is selected, and the update is performed as

$$[\boldsymbol{\theta}_{\rm new}]_n = \Psi\left([\boldsymbol{\theta}^{\rm global}]_n + \eta(t) \cdot \Delta_n\right), \quad n \in \mathcal{I}, \tag{30}$$

where $\Delta_n \sim \mathcal{U}(-\pi, \pi)$ and $\eta(t)$ is an annealed step-size factor defined as

$$\eta(t) = \frac{1}{2}\left(\cos\left(\frac{\pi t}{T}\right) + 1\right). \tag{31}$$

This exploitation phase concentrates the search around promising regions, while the residual stochasticity in Eq. (30) prevents entrapment in shallow local optima.

The complete PC-DOA alternates between exploration and exploitation phases, with elitism employed to retain the best solutions across iterations. The overall procedure is summarized in Algorithm 1.

3.4 Computational complexity and convergence analysis

3.4.1 Computational complexity

The per-iteration cost of PC-DOA is dominated by fitness evaluation in Eq. (25). Each evaluation of $F(\boldsymbol{s}(\boldsymbol{\theta}))$ requires computing $\overline{\mathfrak{D}}$ and $\overline{\mathfrak{E}}$, involving operations on covariance matrices of dimensions $n' \times n'$, where $n' = N + N_{\rm T} - 1$. The determinant, inverse, and trace computations in Eqs. (11)–(13) scale as $\mathcal{O}((n')^3)$. Since $L = MK$ independent components must be evaluated for each candidate, the overall complexity per candidate is $\mathcal{O}(L(n')^3)$. For a population of $N_{\rm p}$ individuals, the per-iteration complexity is $\mathcal{O}(N_{\rm p}L(n')^3)$.

The update operations in Eqs. (28) and (30) require only $\mathcal{O}(N_{\rm p}N)$ computations, which is negligible compared to the fitness evaluation. Therefore, the total computational complexity over T iterations is defined as follows:

$$\mathcal{O}\left(TN_{\rm p}L(n')^3\right). \tag{32}$$

Algorithm 1 Phase-coded dream optimization algorithm

```
Input: Objective function $F : \mathcal{M} \to \mathbb{R}$, waveform parameters $\{N, c\}$, and algorithm parameters $\{N_\mathrm{p}, T, G, \eta, \alpha\}$
Output: Optimal phase vector $\boldsymbol{\theta}^*$ and waveform $\boldsymbol{s}^*$
Initialize population $\mathcal{P}_0 = \{\boldsymbol{\theta}_1^0, \boldsymbol{\theta}_2^0, \ldots, \boldsymbol{\theta}_{N_\mathrm{p}}^0\}$ via hybrid strategy Eqs. (21)–(24), fitness $f(\boldsymbol{\theta}) \leftarrow F(\boldsymbol{s}(\boldsymbol{\theta}))$ for all $\boldsymbol{\theta} \in \mathcal{P}_0$, global best $\boldsymbol{\theta}^* \leftarrow \arg\max_{\boldsymbol{\theta}\in\mathcal{P}_0} f(\boldsymbol{\theta})$, and $f^* \leftarrow f(\boldsymbol{\theta}^*)$
for $t = 1$ to $T$ do
    Initialize $\mathcal{P}_\mathrm{candidate} \leftarrow \varnothing$
    // $\mathcal{P}_\mathrm{candidate}$ denotes the candidate population
    if $t \le \alpha T$ then
        Partition $\mathcal{P}_{t-1}$ into $G$ subgroups
        for each $\boldsymbol{\theta}_\mathrm{old} \in \mathcal{P}_{t-1}$ do
            Generate $\boldsymbol{\theta}_\mathrm{new}$ from $\boldsymbol{\theta}_\mathrm{old}$ via Eq. (28)
            $\mathcal{P}_\mathrm{candidate} \leftarrow \mathcal{P}_\mathrm{candidate} \cup \{\boldsymbol{\theta}_\mathrm{new}\}$
        end for
    else
        for each $\boldsymbol{\theta}_\mathrm{old} \in \mathcal{P}_{t-1}$ do
            Generate $\boldsymbol{\theta}_\mathrm{new}$ guided by $\boldsymbol{\theta}^*$ via Eq. (30)
            $\mathcal{P}_\mathrm{candidate} \leftarrow \mathcal{P}_\mathrm{candidate} \cup \{\boldsymbol{\theta}_\mathrm{new}\}$
        end for
    end if
    Evaluate fitness $f(\boldsymbol{\theta})$ for all $\boldsymbol{\theta} \in \mathcal{P}_\mathrm{candidate}$
    Select next-generation population $\mathcal{P}_t$ from $\mathcal{P}_{t-1} \cup \mathcal{P}_\mathrm{candidate}$
    if $\max_{\boldsymbol{\theta}\in\mathcal{P}_t} f(\boldsymbol{\theta}) > f^*$ then
        $\boldsymbol{\theta}^* \leftarrow \arg\max_{\boldsymbol{\theta}\in\mathcal{P}_t} f(\boldsymbol{\theta})$
        $f^* \leftarrow f(\boldsymbol{\theta}^*)$
    end if
end for
Compute optimal waveform $\boldsymbol{s}^* \leftarrow c \cdot \exp(\mathrm{j}\boldsymbol{\theta}^*)$
Return $\boldsymbol{\theta}^*$ and $\boldsymbol{s}^*$
```

3.4.2 Convergence analysis

The proposed PC-DOA algorithm is a metaheuristic designed to operate over a finite iteration budget T. Its search dynamics are characterized by a deterministic, irreversible transition from an exploration phase to an exploitation phase at $t = \alpha T$. Consequently, its convergence properties are analyzed not in terms of asymptotic global optimality, but through the stability of the solution sequence and the characterization of its limit.

Proposition 2 Let $\{F_t^*\}_{t=0}^T$ be the sequence of the best-found objective values recorded by PC-DOA at iteration t. This sequence is guaranteed to converge to a finite limit $\bar{f}$.

The validity of Proposition 2 is established by two properties:

1. The elitist strategy guarantees the monotonicity of the sequence. The global-best fitness f^* is superseded only if a new candidate solution $\boldsymbol{\theta} \in \mathcal{P}_t$ is found to be strictly superior. This design ensures that $F_{t+1}^* \ge F_t^*$ for all iterations t.

2. The objective space provides a guaranteed upper bound. The objective function $F(\boldsymbol{s})$ is Lipschitz continuous on the compact set $\mathcal{M}$. Therefore, a finite constant $\tau < \infty$ exists such that $F_t^* \le \tau$ for all t.

Given that $\{F_t^*\}$ is both monotonically nondecreasing and bounded above, the monotone convergence theorem rigorously ensures that the sequence converges to a finite limit. Thus, $\lim_{t\to T} F_t^* = \bar{f}$ is guaranteed.

Remark 3 It must be noted that Proposition 2 guarantees stability, not global optimality. The limit $\bar{f}$ is not a fixed theoretical constant but rather the optimal empirical value attainable by the algorithm under its finite budget T. This limit $\bar{f} \le F^*$, where F^* is the global optimum.

The quality of $\bar{f}$ fundamentally depends on the run-specific realization of the stochastic process and the chosen hyperparameters, chiefly the initialization strategy, the population size N_p, and the phase transition point α.

4 Numerical results

This section presents numerical simulations to validate the effectiveness of the proposed PC-DOA and the associated MIUB objective function $F(\boldsymbol{s})$ for constant modulus waveform design.

4.1 Simulation configuration

We consider a complex baseband waveform $\boldsymbol{s} \in \mathbb{C}^N$ of length $N = 64$, normalized to unit energy $E_\mathrm{s} = 1$ (i.e., $c = 1/\sqrt{N}$). The TIR $\boldsymbol{x}$ and clutter $\boldsymbol{w}$ follow zero-mean GMDs. Consistent with cognitive radar design (Bell, 1993; Romero et al., 2011), the mixture parameters $\{\alpha_k, \beta_m, \boldsymbol{Q}_m, \boldsymbol{R}_k\}$ are assumed known a priori. Covariance matrices $\boldsymbol{Q}_m$, $\boldsymbol{R}_k$ are derived from inverse Fourier transforms of the component power spectral densities (PSDs), with $M = K = 2$. The target weights are $\boldsymbol{\beta} = [0.8,\ 0.2]^\mathrm{T}$, and clutter weights $\boldsymbol{\alpha} = [0.2,\ 0.8]^\mathrm{T}$. Representative PSDs are illustrated in Fig. 1 (Yang et al., 2023).

The signal-to-clutter ratio (SCR) is defined as

$$\mathrm{SCR} = 10\lg\left(\frac{\mathrm{tr}(\boldsymbol{Q})}{\mathrm{tr}(\boldsymbol{R})}\right), \tag{33}$$

where $\boldsymbol{Q} = \sum_{m=1}^{2} \beta_m \boldsymbol{Q}_m$ and $\boldsymbol{R} = \sum_{k=1}^{2} \alpha_k \boldsymbol{R}_k$ are the aggregate covariance matrices of the TIR and the clutter-plus-noise, respectively.

The other simulation parameters are given in Table 1.

Table 1 Simulation parameters

Parameter	Value
SCR range	[−5, 5] dB
Population size (N_P)	200
Maximum number of iterations (T)	2000
Init. proportion (η)	0.3
Phase transition (α)	0.9
Number of subgroups (G)	5

The proposed PC-DOA (Algorithm 1) is compared with (1) MI: direct maximization of MI under constant modulus; (2) relative entropy (RE): direct maximization of RE under constant modulus; (3) weighted SCR-MI (WSM): a weighted sum $J_{\mathrm{WSM}}(\boldsymbol{s}) = 0.5 f_{\mathrm{SCR}}(\boldsymbol{s}) + 0.5 f_{\mathrm{MI}}(\boldsymbol{s})$ ($f_{\mathrm{SCR}}(\boldsymbol{s}) = \mathrm{tr}\left(\boldsymbol{R}^{-1}\boldsymbol{SQS}^{\mathrm{H}}\right)$ and $f_{\mathrm{MI}}(\boldsymbol{s}) = \overline{\mathfrak{E}}(\boldsymbol{s})$); (4) random phases coding (RPC): $\theta_n \sim \mathcal{U}[-\pi, \pi)$.

Detection performance is evaluated via receiver operating characteristic (ROC) curves with $10^3/P_{\mathrm{FA}}$ Monte Carlo trials; estimation accuracy is quantified by the MSE of TIR reconstruction as

$$\mathrm{MSE} = \mathbb{E}\left[\|\hat{\boldsymbol{x}} - \boldsymbol{x}\|_2^2\right], \tag{34}$$

where $\hat{\boldsymbol{x}}$ is obtained via matched filtering or minimum MSE estimation.

4.2 Performance analysis

4.2.1 Comparison of optimization objectives

Fig. 2 illustrates the detection performance of waveforms designed according to various optimization criteria. Specifically, Fig. 2(a) depicts the detection probability P_{D} as a function of SCR, with a fixed probability of false alarm $P_{\mathrm{FA}} = 10^{-2}$; Fig. 2(b) presents the ROC curves, which illustrate the relationship between detection probability P_{D} and P_{FA} at an SCR of 0 dB. It is evident that the waveform optimized under the MIUB criterion achieves a slightly higher P_{D} compared to those designed based on the other four criteria across most SCR levels. Moreover, in terms of estimation performance (Fig. 3), it outperforms waveforms designed solely based on MI or RE. Overall, maximizing MIUB not only enhances the target information contained in the echo signal but also enhances the separability between target echoes and clutter. This indicates that MIUB maximization inherently balances detection and parameter estimation performance, while simultaneously improving both.

Beyond detection and estimation, the MIUB-optimized waveform exhibits structural characteristics closely resembling the ambiguity function of LFM. As shown in Fig. 4, the MI-, RE-, and MIUB-based designs achieve more pronounced sidelobe suppression compared with WSM and RPC. Their integrated sidelobe levels (ISL) and peak sidelobe levels (PSL), summarized in Table 2, demonstrate that the MIUB-based waveform achieves the most favorable autocorrelation sidelobe performance, which

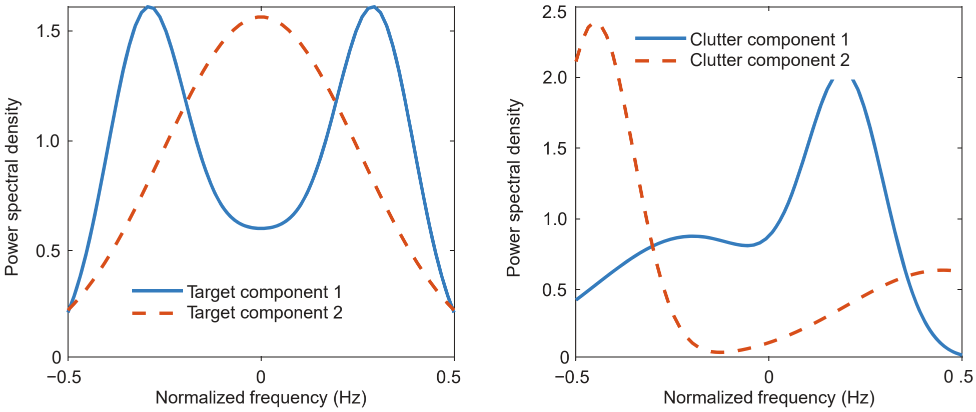

Fig. 1 Simulated PSDs of target and clutter GMDs

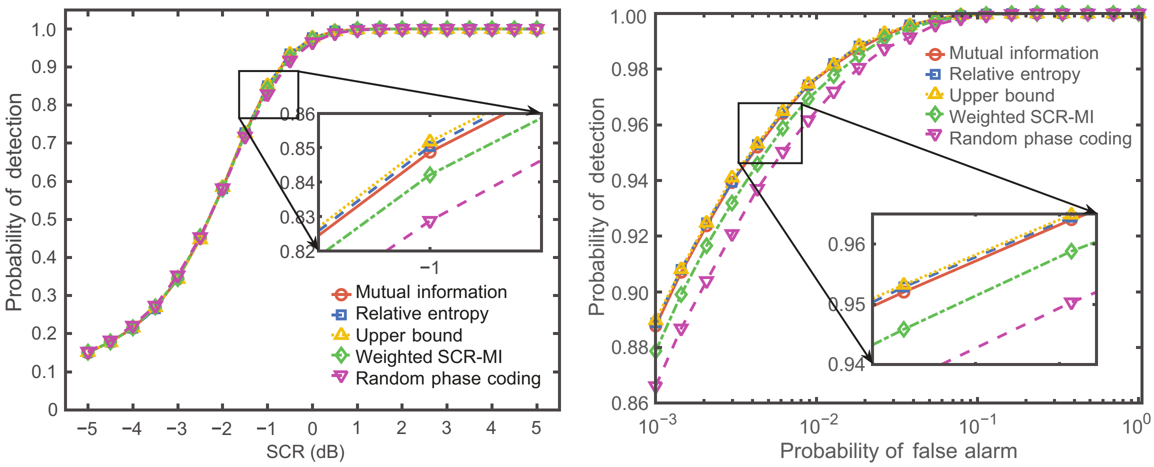

(a) (b)

Fig. 2 Detection performance of waveforms using different criteria: (a) detection probability $P_{\rm D}$ vs. SCR ($P_{\rm FA}=10^{-2}$); (b) ROC curves ($P_{\rm D}$ vs. $P_{\rm FA}$) at SCR = 0 dB

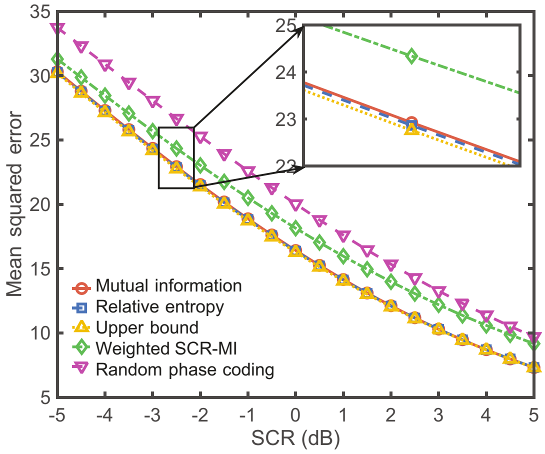

Fig. 3 MSE of TIR estimation vs. SCR for waveforms using different criteria

facilitates the resolution of closely spaced targets while reducing self-induced clutter. Furthermore, Fig. 5 reveals knife-edge ridge structures in the ambiguity function, indicating that the MIUB-based waveform provides high range resolution together with moderate Doppler tolerance. These properties are inherited from the LFM-based initialization and further reinforced during the optimization process.

4.2.2 Comparison of optimization algorithms

Building on the MIUB criterion for waveform design, we further evaluate the performance of PC-DOA in comparison with the standard particle swarm optimization (PSO), whale optimization algorithm (WOA), and grey wolf optimizer (GWO) in terms of detection and parameter estimation, as illustrated in Figs. 6 and 7, respectively. For detection performance, under the constraint of a false alarm probability $P_{\rm FA}=10^{-2}$ and an SCR of 0 dB, PC-DOA consistently outperforms the other three population-based metaheuristics. A similar trend is observed for parameter estimation accuracy. Moreover, the convergence curves in Fig. 8 confirm that PC-DOA not only benefits from superior initialization but also improves steadily and robustly throughout the optimization process, reflecting the advantages of its hybrid initialization and two-stage search strategy.

Table 2 Performance comparison of different waveforms in terms of ISL and PSL

Objective	ISL (dB)	PSL (dB)
MI	−13.290	−24.204
RE	−13.089	−24.292
MIUB	−13.618	−25.279
WSM	−2.545	−12.315
RPC	−0.548	−15.440

4.3 Discussion

The empirical results substantiate the proposed MIUB framework, demonstrating that its principled regularization through the KL divergence term yields a robust balance between detection and estimation performance. The success of PC-DOA in navigating the complex, non-convex search space further underscores a key principle: the co-design of the objective function and a bespoke optimization algorithm

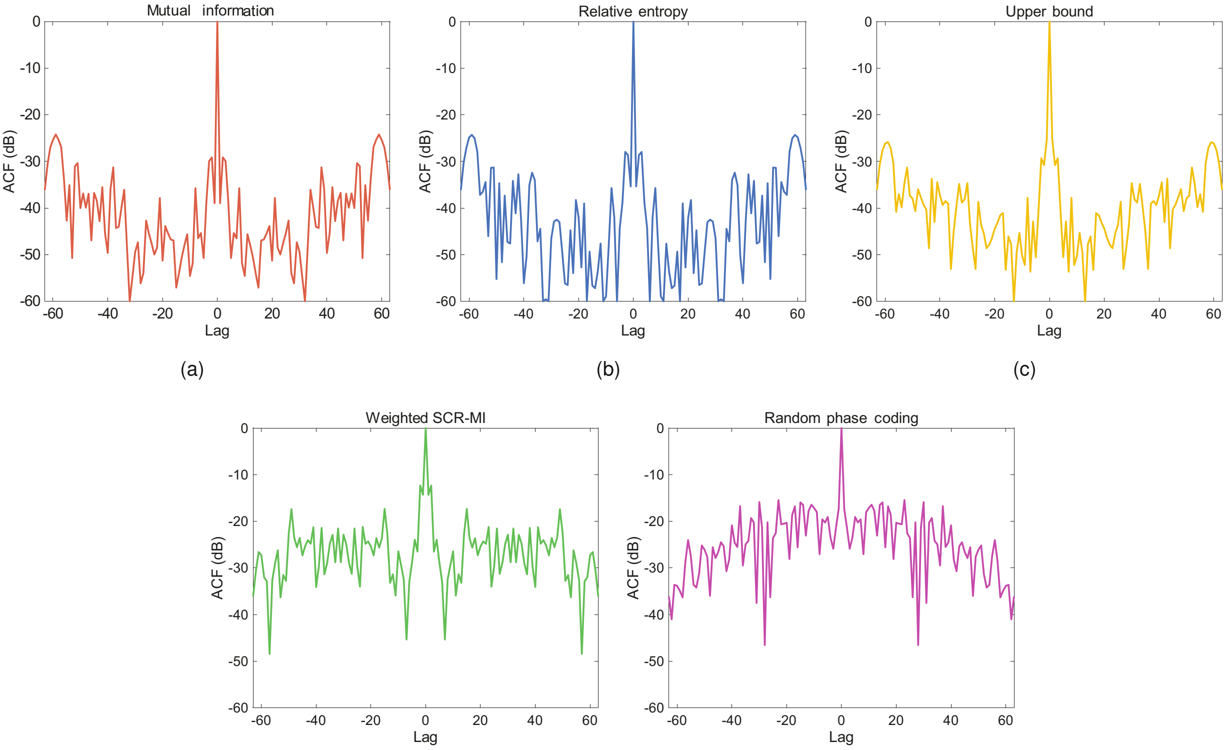

(a) (b) (c)

(d) (e)

Fig. 4 Autocorrelation functions of waveforms using different criteria: (a) MI; (b) RE; (c) MIUB; (d) WSM; (e) RPC

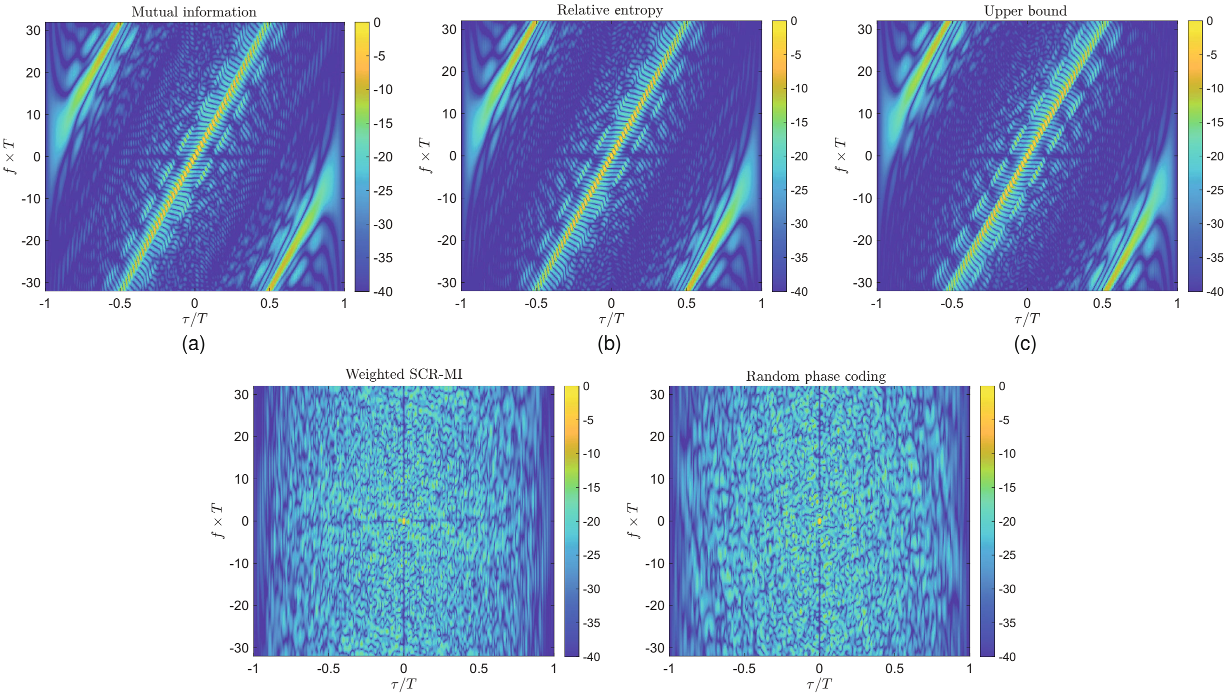

(a) (b) (c)

(d) (e)

Fig. 5 Ambiguity functions of waveforms using different criteria: (a) MI; (b) RE; (c) MIUB; (d) WSM; (e) RPC

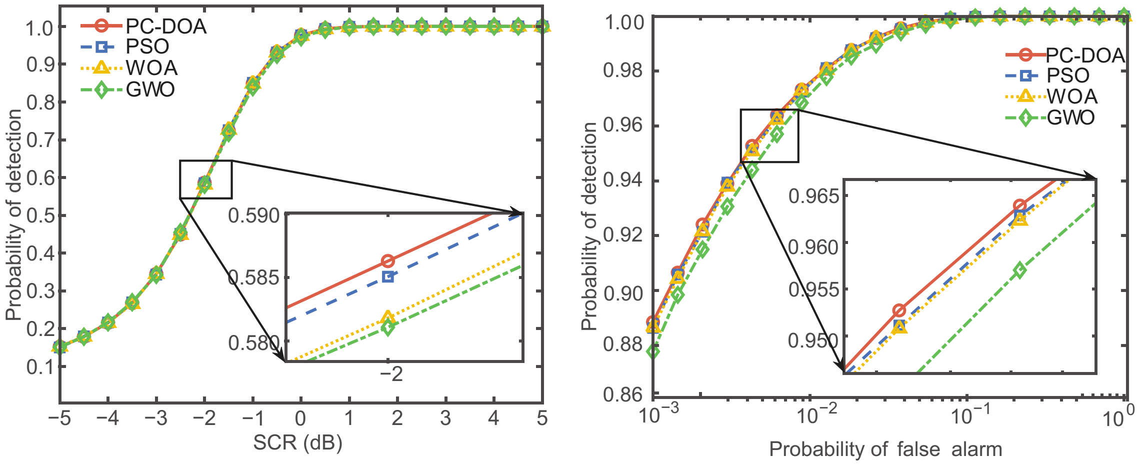

(a) (b)

Fig. 6 Detection performance of waveforms using different optimization algorithms: (a) detection probability vs. SCR ($P_{\mathrm{FA}} = 10^{-2}$); (b) ROC curves ($P_{\mathrm{D}}$ vs. P_{FA}) at SCR = 0 dB

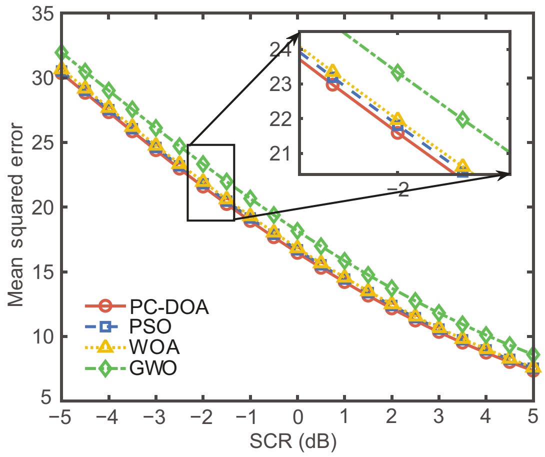

Fig. 7 MSE of TIR estimation vs. SCR of waveforms using different optimization algorithms

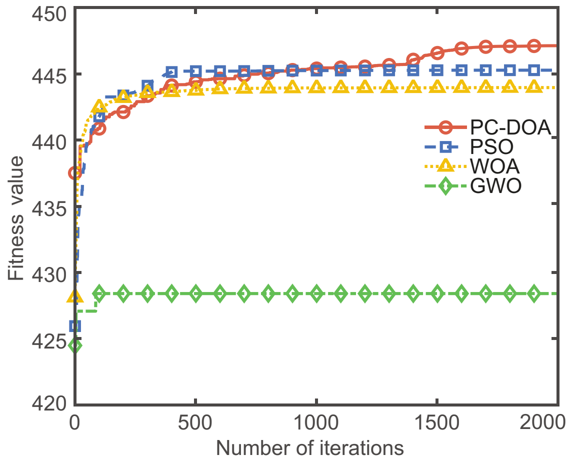

Fig. 8 Convergence of best fitness $F(s)$ optimized using different optimization algorithms

is essential for achieving solutions that approach theoretical performance bounds.

While this work provides a robust framework, its assumptions—namely, the use of GMDs and a quasi-static environment—highlight critical avenues for future research. Key challenges include integrating more powerful data-driven generative models (e.g., variational autoencoders) to capture complex non-Gaussian statistics, extending single-shot optimization to sequential and adaptive frameworks for dynamic scenarios (e.g., via Bayesian filtering loops), and developing computationally efficient surrogate models to enable real-time implementation on hardware-constrained platforms.

5 Conclusions

This work presents a unified information-theoretic framework for constant modulus radar waveform design, jointly optimizing detection and estimation via an MIUB under Gaussian mixture models. To address the ensuing nonconvex optimization, we propose PC-DOA, which leverages hybrid initialization and adaptive bi-phase search on the complex circle manifold. Numerical evaluations confirm that MIUB-based designs outperform conventional baselines, offering superior detection–estimation tradeoffs and desirable ambiguity function properties, thereby establishing a principled foundation for future extensions to more complex and dynamic sensing environments.

Contributors

Ruofeng YU designed the research and processed the data. Ruofeng YU and Chenyang LUO drafted the paper. Shangqu YAN and Mengdi BAI helped organize the paper. Wei YANG and Yaowen FU revised and finalized the paper.

Conflict of interest

All the authors declare that they have no conflict of interest.

Data availability

The data that support the findings of this study are unavailable as no new data were created or analyzed.

References

Bell MR, 1993. Information theory and radar waveform design. *IEEE Trans Inform Theory*, 39(5):1578-1597. https://doi.org/10.1109/18.259642

Blacknell D, 2000. Target detection in correlated SAR clutter. *IEE Proc Radar Son Nav*, 147(1):9. https://doi.org/10.1049/ip-rsn:20000044

Chen XX, Wu H, Cheng YQ, et al., 2023. Joint design of transmit sequence and receive filter based on Riemannian manifold of Gaussian mixture distribution for MIMO radar. *IEEE Trans Geosci Remote Sens*, 61:5102213. https://doi.org/10.1109/TGRS.2023.3257643

DeLong D, Hofstetter E, 1970. Optimum radar signal-filter pairs in a cluttered environment. *IEEE Trans Inform Theory*, 16(1):89-90. https://doi.org/10.1109/TIT.1970.1054412

Goldberger, Gordon, Greenspan, 2003. An efficient image similarity measure based on approximations of KL-divergence between two Gaussian mixtures. Proc 9th IEEE Int Conf on Computer Vision, p.487-493. https://doi.org/10.1109/ICCV.2003.1238387

Gu YJ, Goodman NA, 2019. Information-theoretic waveform design for Gaussian mixture radar target profiling. *IEEE Trans Aerosp Electron Syst*, 55(3):1528-1536. https://doi.org/10.1109/TAES.2018.2881365

Guerci JR, Guerci RM, Ranagaswamy M, et al., 2014. CoFAR: cognitive fully adaptive radar. Proc IEEE Radar Conf, p.984-989. https://doi.org/10.1109/RADAR.2014.6875736

Gui RH, Wang WQ, Cui C, et al., 2018. Coherent pulsed-FDA radar receiver design with time-variance consideration: SINR and CRB analysis. *IEEE Trans Signal Process*, 66(1):200-214. https://doi.org/10.1109/TSP.2017.2764860

Hao TD, Cui C, Gong Y, 2019. Efficient waveform design method for target estimation under the detection and peak-to-average power ratio constraints in cognitive radar. *IEEE Access*, 7:21300-21309. https://doi.org/10.1109/ACCESS.2019.2898219

Haykin S, 2006. Cognitive radar: a way of the future. *IEEE Signal Process Mag*, 23(1):30-40. https://doi.org/10.1109/MSP.2006.1593335

Idriss Z, Raj RG, Narayanan RM, 2021. Waveform optimization for multistatic radar imaging using mutual information. *IEEE Trans Aerosp Electron Syst*, 57(4):2410-2425. https://doi.org/10.1109/TAES.2021.3061811

Jiu B, Liu HW, Zhang L, et al., 2015. Wideband cognitive radar waveform optimization for joint target radar signature estimation and target detection. *IEEE Trans Aerosp Electron Syst*, 51(2):1530-1546. https://doi.org/10.1109/TAES.2015.130847

Levanon N, Mozeson E, 2004. Radar Signals. John Wiley & Sons, Inc., New York, USA. https://doi.org/10.1002/0471663085

Poole B, Ozair S, Van Den Oord A, et al., 2019. On variational bounds of mutual information. Proc 36th Int Conf on Machine Learning, p.5171-5180.

Romero RA, Bae J, Goodman NA, 2011. Theory and application of SNR and mutual information matched illumination waveforms. *IEEE Trans Aerosp Electron Syst*, 47(2):912-927. https://doi.org/10.1109/TAES.2011.5751234

Shen TL, Lu JB, Zhang YL, et al., 2024. Waveform design of cognitive MIMO radar with multiple targets and multiple criterias. 6th Int Conf on Information Science, Electrical and Automation Engineering, 13275:1327510. https://doi.org/10.1117/12.3037769

Skolnik M, 2008. An Introduction and Overview of Radar. McGraw-Hill, New York, USA, p.1.

Tang B, Naghsh MM, Tang J, 2015. Relative entropy-based waveform design for MIMO radar detection in the presence of clutter and interference. *IEEE Trans Signal Process*, 63(14):3783-3796. https://doi.org/10.1109/TSP.2015.2423257

Tang B, Zhang Y, Tang J, 2018. An efficient minorization maximization approach for MIMO radar waveform optimization via relative entropy. *IEEE Trans Signal Process*, 66(2):400-411. https://doi.org/10.1109/TSP.2017.2771726

Thornton CE, Kozy MA, Buehrer RM, et al., 2020. Deep reinforcement learning control for radar detection and tracking in congested spectral environments. *IEEE Trans Cogn Commun Netw*, 6(4):1335-1349. https://doi.org/10.1109/TCCN.2020.3019605

van der Werf I, Hendriks RC, Heusdens R, et al., 2023. Transmit waveform design based on the Cramér-Rao lower bound. Proc 9th IEEE Int Workshop on Computational Advances in Multi-Sensor Adaptive Processing, p.166-170. https://doi.org/10.1109/CAMSAP58249.2023.10403457

Xiao Y, Hu XX, 2022. Waveform design for multi-target detection based on two-stage information criterion. *Entropy*, 24(8):1075. https://doi.org/10.3390/e24081075

Xu Z, Xie Z, Fan CY, et al., 2022. Probabilistically robust radar waveform design for extended target detection. *IEEE Trans Signal Process*, 70:4212-4224. https://doi.org/10.1109/TSP.2022.3198185

Xu Z, Tang B, Ai WH, et al., 2025a. Radar transceiver design for extended targets based on optimal linear detector. *IEEE Trans Aerosp Electron Syst*, 61(3):6070-6082. https://doi.org/10.1109/TAES.2024.3524951

Xu Z, Tang B, Ai WH, et al., 2025b. Relative entropy based jamming signal design against radar target detection. *IEEE Trans Signal Process*, 73:1200-1215. https://doi.org/10.1109/TSP.2025.3544305

Yang C, Yang W, Qiu XF, et al., 2023. Cognitive radar waveform design method under the joint constraints of transmit energy and spectrum bandwidth. *Remote Sens*, 15(21):5187.
https://doi.org/10.3390/rs15215187

Yu RF, Fu YW, Yang W, et al., 2024. Waveform design for target information maximization over a complex circle manifold. *Remote Sens*, 16(4):645.
https://doi.org/10.3390/rs16040645

Zhu ZH, Kay S, Raghavan RS, 2017. Information-theoretic optimal radar waveform design. *IEEE Signal Process Lett*, 24(3):274-278.
https://doi.org/10.1109/LSP.2017.2655879

Appendix A: Approximation error bounds for MI and KL divergence

1. Error bound for the MI approximation

The MI is defined as $I(\boldsymbol{x};\boldsymbol{y}) = h(\boldsymbol{y}) - h(\boldsymbol{y}|\boldsymbol{x})$, where $h(\cdot)$ denotes the differential entropy. Our approximation, $\overline{\mathfrak{E}}(\boldsymbol{s})$, replaces the true entropy term $h(\boldsymbol{y}) = -\mathbb{E}_{\boldsymbol{y}}[\ln p_1(\boldsymbol{y})]$ with the surrogate term $\tilde{h}(\boldsymbol{y}) = -\ln p_1(\boldsymbol{y}_0)$, where $\boldsymbol{y}_0 = \mathbb{E}[\boldsymbol{y}]$. For the zero-mean processes considered, $\boldsymbol{y}_0 = \boldsymbol{0}$. The approximation error is therefore defined as

$$\Delta h = h(\boldsymbol{y}) - \tilde{h}(\boldsymbol{y}). \tag{A1}$$

To quantify this error, we define the log-likelihood function $\phi(\boldsymbol{y}) = \ln p_1(\boldsymbol{y})$ and perform a second-order Taylor expansion around the mean $\boldsymbol{y}_0 = \boldsymbol{0}$ as follows:

$$\phi(\boldsymbol{y}) = \phi(\boldsymbol{0}) + (\nabla\phi(\boldsymbol{0}))^{\mathrm{H}}\boldsymbol{y} + \frac{1}{2}\boldsymbol{y}^{\mathrm{H}}\boldsymbol{H}(\boldsymbol{0})\boldsymbol{y} + R_3(\boldsymbol{y}), \tag{A2}$$

where $\boldsymbol{H}(\boldsymbol{0})$ is the Hessian matrix of $\phi(\boldsymbol{y})$ evaluated at the origin and $R_3(\boldsymbol{y})$ represents the higher-order remainder terms. Taking the expectation with respect to $\boldsymbol{y} \sim p_1(\boldsymbol{y})$ yields

$$\begin{aligned}\mathbb{E}[\phi(\boldsymbol{y})] =& \phi(\boldsymbol{0}) + (\nabla\phi(\boldsymbol{0}))^{\mathrm{H}}\mathbb{E}[\boldsymbol{y}] \\ &+ \frac{1}{2}\mathbb{E}[\boldsymbol{y}^{\mathrm{H}}\boldsymbol{H}(\boldsymbol{0})\boldsymbol{y}] + \mathbb{E}[R_3(\boldsymbol{y})].\end{aligned} \tag{A3}$$

Since $\mathbb{E}[\boldsymbol{y}] = \boldsymbol{0}$, the first-order term vanishes. By neglecting the expectation of the remainder, $\mathbb{E}[R_3(\boldsymbol{y})]$, the dominant error term is derived from $h(\boldsymbol{y}) = -\mathbb{E}[\phi(\boldsymbol{y})]$ and $\tilde{h}(\boldsymbol{y}) = -\phi(\boldsymbol{0})$.

$$\begin{aligned}\Delta h &\approx -\frac{1}{2}\mathbb{E}[\boldsymbol{y}^{\mathrm{H}}\boldsymbol{H}(\boldsymbol{0})\boldsymbol{y}] = -\frac{1}{2}\mathbb{E}\left[\mathrm{tr}\left(\boldsymbol{H}(\boldsymbol{0})\boldsymbol{y}\boldsymbol{y}^{\mathrm{H}}\right)\right] \\ &= -\frac{1}{2}\mathrm{tr}\left(\boldsymbol{H}(\boldsymbol{0})\mathbb{E}[\boldsymbol{y}\boldsymbol{y}^{\mathrm{H}}]\right) = -\frac{1}{2}\mathrm{tr}\left(\boldsymbol{H}(\boldsymbol{0})\boldsymbol{C}_{\boldsymbol{y}}\right),\end{aligned} \tag{A4}$$

where $\boldsymbol{C}_{\boldsymbol{y}} = \sum_{\ell=1}^{L}\gamma_\ell\boldsymbol{\Sigma}_\ell$ is the aggregate covariance matrix of $\boldsymbol{y}$ under hypothesis $\mathcal{H}_1$.

The magnitude of the error can be bounded using matrix norm inequalities. Applying the Cauchy–Schwarz inequality for the Hilbert–Schmidt inner product, $|\mathrm{tr}(\boldsymbol{A}\boldsymbol{B})| \le \|\boldsymbol{A}\|_{\mathrm{F}}\|\boldsymbol{B}\|_{\mathrm{F}}$, yields

$$|\Delta h| \le \frac{1}{2}\|\boldsymbol{H}(\boldsymbol{0})\|_{\mathrm{F}}\|\boldsymbol{C}_{\boldsymbol{y}}\|_{\mathrm{F}}, \tag{A5}$$

where $\|\boldsymbol{A}\|_{\mathrm{F}}$ denotes the Frobenius norm of matrix $\boldsymbol{A}$.

If the spectral norm of the Hessian matrix is bounded by $\|\boldsymbol{H}(\boldsymbol{0})\|_2 \le L_{\mathrm{H}}$, we can use the relation $\|\boldsymbol{A}\|_{\mathrm{F}} \le \sqrt{\mathrm{rank}(\boldsymbol{A})}\|\boldsymbol{A}\|_2$ to obtain

$$|\Delta h| \le \frac{\sqrt{n'}L_{\mathrm{H}}}{2}\|\boldsymbol{C}_{\boldsymbol{y}}\|_{\mathrm{F}}, \tag{A6}$$

where $n' = N + N_{\mathrm{T}} - 1$.

Furthermore, for a positive semi-definite matrix $\boldsymbol{C}_{\boldsymbol{y}}$, the inequality $|\mathrm{tr}(\boldsymbol{A}\boldsymbol{B})| \le \|\boldsymbol{A}\|_2\mathrm{tr}(\boldsymbol{B})$ provides an alternative bound as follows:

$$|\Delta h| \le \frac{L_{\mathrm{H}}}{2}\mathrm{tr}(\boldsymbol{C}_{\boldsymbol{y}}). \tag{A7}$$

These bounds collectively show that the approximation is accurate when the signal's total variance is small.

2. Error bound for the KL divergence approximation

The exact KL divergence is $\mathcal{D}_{\mathrm{KL}}(p_1 \parallel p_0) = \int p_1(\boldsymbol{y})\ln\frac{p_1(\boldsymbol{y})}{p_0(\boldsymbol{y})}\mathrm{d}\boldsymbol{y}$. The approximation error is defined as

$$\Delta\mathcal{D} = \mathcal{D}_{\mathrm{KL}}(p_1 \parallel p_0) - \overline{\mathfrak{D}}(\boldsymbol{s}), \tag{A8}$$

which can be decomposed as follows:

$$\begin{aligned}\Delta\mathcal{D} =& \underbrace{\sum_{\ell=1}^{L}\gamma_\ell\mathbb{E}_{p_1^{(\ell)}}\left[\ln\frac{p_1(\boldsymbol{y})}{\gamma_\ell p_1^{(\ell)}(\boldsymbol{y})}\right]}_{\Delta_{\mathrm{num}}} \\ &+ \underbrace{\sum_{\ell=1}^{L}\gamma_\ell\mathbb{E}_{p_1^{(\ell)}}\left[\ln\frac{\alpha_{k^\star(\ell)}p_0^{(k^\star(\ell))}(\boldsymbol{y})}{p_0(\boldsymbol{y})}\right]}_{\Delta_{\mathrm{den}}}.\end{aligned} \tag{A9}$$

This decomposition separates the total approximation error into two distinct terms: the numerator-induced discrepancy (Δ_{num}) and the denominator-induced discrepancy (Δ_{den}). The former originates from inter-component contributions of p_1, while the latter arises from component-assignment mismatch and inter-component effects in p_0. By construction, the signs of these error terms are fixed and invariant.

For Δ_{num}, the argument of the logarithm is

$$\frac{\sum_m \gamma_m p_1^{(m)}(\boldsymbol{y})}{\gamma_\ell p_1^{(\ell)}(\boldsymbol{y})} = 1 + \sum_{m\neq\ell} \frac{\gamma_m p_1^{(m)}(\boldsymbol{y})}{\gamma_\ell p_1^{(\ell)}(\boldsymbol{y})} \geq 1, \quad \text{(A10)}$$

which implies $\Delta_{\text{num}} \geq 0$.

For Δ_{den}, the argument is

$$\frac{\alpha_{k^\star(\ell)} p_0^{(k^\star(\ell))}(\boldsymbol{y})}{\sum_k \alpha_k p_0^{(k)}(\boldsymbol{y})} \in (0, 1], \quad \text{(A11)}$$

implying $\Delta_{\text{den}} \leq 0$.

The total error is bounded by the magnitudes of its components. We bound the dominant term, $|\Delta_{\text{den}}|$, using the inequality $\ln(1+x) \leq x$ for $x \geq 0$, which is expressed as

$$\begin{aligned}
&|\Delta_{\text{den}}| = -\Delta_{\text{den}} \\
&= \sum_{\ell=1}^{L} \gamma_\ell \mathbb{E}_{p_1^{(\ell)}} \left[\ln \left(1 + \sum_{k\neq k^\star(\ell)} \frac{\alpha_k p_0^{(k)}(\boldsymbol{y})}{\alpha_{k^\star(\ell)} p_0^{(k^\star(\ell))}(\boldsymbol{y})} \right) \right] \\
&\leq \sum_{\ell=1}^{L} \gamma_\ell \mathbb{E}_{p_1^{(\ell)}} \left[\sum_{k\neq k^\star(\ell)} \frac{\alpha_k p_0^{(k)}(\boldsymbol{y})}{\alpha_{k^\star(\ell)} p_0^{(k^\star(\ell))}(\boldsymbol{y})} \right] \\
&= \sum_{\ell=1}^{L} \sum_{k\neq k^\star(\ell)} \frac{\gamma_\ell \alpha_k}{\alpha_{k^\star(\ell)}} \int p_1^{(\ell)}(\boldsymbol{y}) \frac{p_0^{(k)}(\boldsymbol{y})}{p_0^{(k^\star(\ell))}(\boldsymbol{y})} \mathrm{d}\boldsymbol{y}.
\end{aligned} \quad \text{(A12)}$$

The integral is governed by the overlap between the Gaussian densities. When the KL divergence between components is large, this term is exponentially suppressed. This leads to the approximate bound defined as

$$|\Delta\mathcal{D}| \leq O\left(\sum_{\ell=1}^{L} \gamma_\ell \sum_{k\neq k^\star(\ell)} \alpha_k \mathrm{e}^{-\mathcal{D}_{\text{KL}}(p_1^{(\ell)} \| p_0^{(k)})} \right), \quad \text{(A13)}$$

where $O(z)$ denotes the approximation error $|\Delta\mathcal{D}|$ is asymptotically upper bounded by the order of z.

This confirms that the approximation is accurate when the GMD components are well-separated.

Appendix B: Proof of Proposition 1

We prove that the objective function

$$F(\boldsymbol{s}) = \overline{\mathfrak{D}}(\boldsymbol{s}) + \overline{\mathfrak{E}}(\boldsymbol{s}) \quad \text{(B1)}$$

is Lipschitz continuous on the feasible set $\mathcal{M} = \{\boldsymbol{s} \in \mathbb{C}^N : |\boldsymbol{s}_n| = c, \forall n\}$.

Assume that the component covariance matrices $\{\boldsymbol{R}_k\}$ and $\{\boldsymbol{Q}_m\}$ are positive definite, with eigenvalues bounded in $[\lambda_{\min}, \lambda_{\max}]$, where $\lambda_{\min} > 0$. This ensures that for any $\boldsymbol{s} \in \mathcal{M}$, the composite covariance matrix $\boldsymbol{\Sigma}_\ell(\boldsymbol{s})$ is positive definite, with its eigenvalues bounded in a compact interval $[\lambda'_{\min}, \lambda'_{\max}]$.

1. Lipschitz continuity of the composite covariance matrix

Let $\boldsymbol{s}_1, \boldsymbol{s}_2 \in \mathcal{M}$. The mapping from a vector to its matrix form, $\boldsymbol{s} \mapsto \boldsymbol{S}(\boldsymbol{s})$, is linear. For a Toeplitz structure, this mapping satisfies

$$\|\boldsymbol{S}(\boldsymbol{s}_1) - \boldsymbol{S}(\boldsymbol{s}_2)\|_{\text{F}} = \sqrt{N_{\text{T}}} \|\boldsymbol{s}_1 - \boldsymbol{s}_2\|_2. \quad \text{(B2)}$$

The difference in the composite covariance is obtained by

$$\begin{aligned}
\boldsymbol{\Sigma}_\ell(\boldsymbol{s}_1) - \boldsymbol{\Sigma}_\ell(\boldsymbol{s}_2) =& (\boldsymbol{S}_1 - \boldsymbol{S}_2) \boldsymbol{Q}_m \boldsymbol{S}_1^{\text{H}} \\
&+ \boldsymbol{S}_2 \boldsymbol{Q}_m \left(\boldsymbol{S}_1^{\text{H}} - \boldsymbol{S}_2^{\text{H}} \right).
\end{aligned} \quad \text{(B3)}$$

Applying the triangle and submultiplicative properties of the Frobenius norm, and noting that $\|\boldsymbol{S}_1\|_{\text{F}} = \|\boldsymbol{S}_2\|_{\text{F}} = \sqrt{N_{\text{T}} E_{\text{s}}}$ for some constant E_{s}, we have

$$\begin{aligned}
&\|\boldsymbol{\Sigma}_\ell(\boldsymbol{s}_1) - \boldsymbol{\Sigma}_\ell(\boldsymbol{s}_2)\|_{\text{F}} \\
&\quad \leq 2 \|\boldsymbol{S}_1 - \boldsymbol{S}_2\|_{\text{F}} \|\boldsymbol{Q}_m\|_{\text{F}} \|\boldsymbol{S}_1\|_{\text{F}} \\
&\quad \leq \left(2\sqrt{N_{\text{T}}} (\sqrt{N_{\text{T}}} \lambda_{\max}) \sqrt{N_{\text{T}} E_{\text{s}}} \right) \|\boldsymbol{s}_1 - \boldsymbol{s}_2\|_2 \\
&\quad = \left(2 N_{\text{T}}^{3/2} \sqrt{E_{\text{s}}} \lambda_{\max} \right) \|\boldsymbol{s}_1 - \boldsymbol{s}_2\|_2.
\end{aligned} \quad \text{(B4)}$$

Thus, the map $\boldsymbol{s} \mapsto \boldsymbol{\Sigma}_\ell(\boldsymbol{s})$ is Lipschitz continuous with constant

$$L_\Sigma = 2 N_{\text{T}}^{3/2} \sqrt{E_{\text{s}}} \lambda_{\max}. \quad \text{(B5)}$$

2. Lipschitz continuity of the objective function components

The objective $F(\boldsymbol{s})$ is a sum of functions that are compositions of Lipschitz continuous functions over the compact domain $\mathcal{M}$. Standard results from matrix analysis confirm that, for positive definite matrices on a compact set, maps like $\boldsymbol{A} \mapsto \det(\boldsymbol{A})$, $\boldsymbol{A} \mapsto \ln\det(\boldsymbol{A})$, and $\boldsymbol{A} \mapsto \boldsymbol{A}^{-1}$ are Lipschitz continuous.

(1) MI term

The MI approximation is

$$\overline{\mathfrak{E}}(\boldsymbol{s}) = C - \ln G(\boldsymbol{s}), \quad \text{(B6)}$$

where $G(\boldsymbol{s})=\sum_{\ell}\gamma_{\ell}\det(\boldsymbol{\Sigma}_{\ell}(\boldsymbol{s}))^{-1}$.

Let $C_{\mathrm{det},\ell}$ be the Lipschitz constant for the map $\boldsymbol{\Sigma}\mapsto(\det(\boldsymbol{\Sigma}))^{-1}$ over the compact set of attainable covariance matrices. The constant for $G(\boldsymbol{s})$ is obtained by

$$L_{\mathrm{G}}=L_{\Sigma}\sum_{\ell=1}^{L}\gamma_{\ell}C_{\mathrm{det},\ell}. \tag{B7}$$

Since $\mathcal{M}$ is compact, $G(\boldsymbol{s})$ is bounded below by a positive minimum value $G_{\min}>0$. The function $-\ln(x)$ is Lipschitz continuous on $[G_{\min},\infty)$ with constant $1/G_{\min}$. By the chain rule for Lipschitz functions, the Lipschitz constant for $\overline{\mathfrak{E}}(\boldsymbol{s})$ is defined as

$$L_{\overline{\mathrm{E}}}=\frac{L_{\mathrm{G}}}{G_{\min}}=\frac{L_{\Sigma}}{G_{\min}}\sum_{\ell=1}^{L}\gamma_{\ell}C_{\mathrm{det},\ell}. \tag{B8}$$

(2) KL term

This term is a weighted sum of

$$J(k^{\star}(\ell),\ell,\boldsymbol{s})=\min_{k}J(k,\ell,\boldsymbol{s}), \tag{B9}$$

where

$$\begin{aligned}J(k,\ell,\boldsymbol{s})=&\operatorname{tr}(\boldsymbol{R}_k^{-1}\boldsymbol{\Sigma}_{\ell}(\boldsymbol{s}))\\&-\ln\det(\boldsymbol{R}_k^{-1}\boldsymbol{\Sigma}_{\ell}(\boldsymbol{s}))+C_{k,\ell}.\end{aligned} \tag{B10}$$

The trace part is Lipschitz with constant $\|\boldsymbol{R}_k^{-1}\|_{\mathrm{F}}L_{\Sigma}$. For the log-determinant part, the inequality $|\ln\det(\boldsymbol{A})-\ln\det(\boldsymbol{B})|\le\|\boldsymbol{A}^{-1}\|_2\|\boldsymbol{A}-\boldsymbol{B}\|_{\mathrm{F}}$ implies that the term $-\ln\det(\boldsymbol{\Sigma}_{\ell}(\boldsymbol{s}))$ is Lipschitz with constant $(1/\lambda'_{\min})L_{\Sigma}$. Thus, each $J(k,\ell,\boldsymbol{s})$ is Lipschitz with constant

$$L_{\mathrm{j},k,\ell}=\left(\left\|\boldsymbol{R}_k^{-1}\right\|_{\mathrm{F}}+\frac{1}{\lambda'_{\min}}\right)L_{\Sigma}. \tag{B11}$$

The minimum of a finite set of Lipschitz functions is also Lipschitz, with a constant bounded by the maximum of the individual constants. Therefore, the Lipschitz constant for the KL term is defined as

$$L_{\overline{\mathrm{D}}}=\sum_{\ell=1}^{L}\gamma_{\ell}\left(\max_{k}L_{\mathrm{j},k,\ell}\right). \tag{B12}$$

Since both $\overline{\mathfrak{E}}(\boldsymbol{s})$ and $\overline{\mathfrak{D}}(\boldsymbol{s})$ are Lipschitz continuous on the compact set $\mathcal{M}$, their sum $F(\boldsymbol{s})$ is also Lipschitz continuous. An upper bound for its Lipschitz constant is obtained by the sum of the individual constants

$$L_{\mathrm{F}}=L_{\overline{\mathrm{E}}}+L_{\overline{\mathrm{D}}}. \tag{B13}$$